The Astrophysical Journal, 811:80 (14pp), 2015 October 1 doi:10.1088/0004-637X/811/2/80

THE FORMATION OF *IRIS* DIAGNOSTICS. V. A QUINTESSENTIAL MODEL ATOM OF C II AND GENERAL FORMATION PROPERTIES OF THE C II LINES AT 133.5 nm

Bhavna Rathore and Mats Carlsson
Institute of Theoretical Astrophysics, University of Oslo, P.O. Box 1029 Blindern, N-0315 Oslo, Norway; bhavna.rathore@astro.uio.no, mats.carlsson@astro.uio.no
Received 2015 June 5; accepted 2015 August 4; published 2015 September 24

ABSTRACT

The C II 133.5 nm lines are important observables for the NASA/SMEX mission *Interface Region Imaging Spectrograph*. To make three-dimensional (3D) non-LTE radiative transfer computationally feasible, it is crucial to have a model atom with as few levels as possible while retaining the main physical processes. We here develop such a model atom and we study the general formation properties of the C II lines. We find that a nine-level model atom of C I–C III with the transitions treated assuming complete frequency redistribution (CRD) suffices to describe the C II 133.5 nm lines. 3D scattering effects are important for the intensity in the core of the line. The lines are formed in the optically thick regime. The core intensity is formed in layers where the temperature is about 10 kK at the base of the transition region. The lines are 1.2–4 times wider than the atomic absorption profile due to the formation in the optically thick regime. The smaller opacity broadening happens for single peak intensity profiles where the chromospheric temperature is low with a steep source function increase into the transition region, the larger broadening happens when there is a temperature increase from the photosphere to the low chromosphere leading to a local source function maximum and a double peak intensity profile with a central reversal. Assuming optically thin formation with the standard coronal approximation leads to several errors: neglecting photoionization severly underestimates the amount of C II at temperatures below 16 kK, erroneously shifts the formation from 10 kK to 25 kK, and leads to too low intensities.

Key words: line: formation – radiative transfer – Sun: atmosphere – Sun: chromosphere – Sun: transition region

1. INTRODUCTION

In radiative equilibrium, the temperature naturally decreases with height. It therefore came as a surprise when it was realized that the solar outer atmosphere shows a temperature increase, from about 6000 K at the visible surface to millions of degrees in the corona. It is clear that the energy necessary to sustain these high temperatures originates in the solar convection zone but the mechanisms of transportation and dissipation of the energy to the outer solar atmosphere are still hotly debated.

The solar chromosphere—the region a few thousand kilometers thick between the solar photosphere and the transition region and corona—plays a central role in this puzzle. This is the region where we go from a magnetic field being pushed around by the plasma motions in the lower parts (high value of plasma β, the ratio of the gas pressure to the magnetic pressure) to a region where the magnetic pressure dominates. The energy that heats the solar corona needs to be transported through the chromosphere. The total energy needed to balance the radiative losses in the chromosphere is also at least 10 times larger than what is needed to sustain a hot corona (Withbroe & Noyes 1977).

In order to spectroscopically diagnose the chromosphere, we need spectral lines with high enough opacity to have the formation there. This means resonance lines of abundant elements from the ionization state that dominates under chromospheric conditions or lines from excited levels of hydrogen or helium. In the optical part of the spectrum, accessible from ground based observatories, we are restricted to a handful of spectral lines that meet these criteria: the most important being the hydrogen H-α line, the resonance lines and infrared triplet lines from singly ionized calcium, and the helium 1083 nm line. These diagnostic lines have provided a wealth of information on the solar chromosphere, but there are challenges in the interpretation of the observations: the Hα line has a very large thermal width and is a very strongly scattering line, largely decoupled from the local conditions (Leenaarts et al. 2012), the calcium lines carry the chromospheric signal only in the core of a strong photospheric absorption line and the interpretation is heavily dependent on numerical modeling (Carlsson & Stein 1997), while the helium 1083 nm line has a complicated formation with a lower level that is mainly populated from ionization from coronal radiation followed by recombination.

The ultraviolet (UV) part of the spectrum provides many more diagnostic possibilities for chromospheric studies. There are many resonance lines from abundant elements in this part of the spectrum, the continuum radiation is much fainter in the UV, and the chromospheric diagnostics are intrinsically stronger. The recently launched NASA/SMEX mission *Interface Region Imaging Spectrograph* (*IRIS*) was especially designed to target the solar chromosphere and transition region (De Pontieu et al. 2014). *IRIS* provides high spectral, spatial, and temporal resolution in three wavelength bands: 133.2–135.8 nm and 138.9–140.7 nm with 1.3 pm wavelength pixels (corresponding to 2.9–2.7 km s^{-1}) and 278.3–283.4 nm with 2.5 pm wavelength pixels (2.7 km s^{-1}), 0.167 arcsec spatial pixels and 0.33 arcsec slit width.

The resonance lines from singly ionized carbon (C II) around 133.5 nm are among the strongest lines in the solar UV spectrum. There are three components in the multiplet: at 133.4532 nm and at 133.5708 nm, with a weaker blend at 133.5663 nm. The large number of photons emitted in the lines makes it possible to observe at high spatial and temporal resolution and the C II lines are therefore among the more important diagnostic lines for *IRIS*. To explore this diagnostic potential, it is important to find out how the lines are formed and thereby establish how the conditions in the solar outer

atmosphere are encoded in the line profiles. Singly ionized carbon is the dominant ionization state throughout most of the upper chromosphere, but C II also exists in significant amounts up to middle transition region temperatures, as we will show here.

The very first C II solar spectrum was taken by the normal-incidence grating spectrograph from the US Naval Research Laboratory on 1960 April 19 (Detwiler et al. 1961). Later, the lines were observed several times from the series of *OSO* satellites, especially *OSO*-4, though this instrument only obtained barely resolved C II spectra (Pottasch 1964). These authors suggested that the primary emission comes from regions with temperatures of 20 kK. Later, Chipman (1971) used *OSO*-4 and *OSO*-6 observations of the C II lines to constrain the temperature in the upper chromosphere and found the observations to be compatible with a temperature plateau at about 15 kK. Lites et al. (1978) used *OSO*-8 observations to constrain the temperature structure of the upper chromosphere using center-to-limb measurements of the C II lines. Through spectrum synthesis of the lines, they found them to be extremely sensitive to the temperature and physical extent of the plateau at 20 kK proposed by Vernazza et al. (1973) and found the observations to be more compatible with a plateau at 16.5 kK with 25% more material than in the models by Vernazza et al. (1973). The *OSO*-8 observations reported on by Lites et al. (1978) were the highest spectral resolution observations thus far and the average quiet-Sun profiles show a clear central reversal and a red emission peak slightly brighter than the blue peak.

A detailed discussion of the formation of the C II 133.5 nm multiplet appears in Avrett & Loeser (2008). This study is based on a one-dimensional (1D), time-independent semi-empirical model constructed to reproduce the average quiet-Sun observations presented in the SUMER atlas of the extreme UV spectrum (Curdt et al. 2001). Avrett et al. (2013) presented further calculations of the C II 133.5 nm multiplet in four semiempirical models representing the faint and mean internetwork, a network lane, and bright network.

The C II lines have also been used to diagnose other stars. Brown & Carpenter (1984) used them to constrain the chromospheric temperature structure in late-type giant and supergiant stars. The C II multiplet is also considered as a good diagnostic to estimate stellar basal fluxes (Schrijver 1995). A comprehensive study based on the analysis of time series data with the Solar Ultraviolet Measurement of Emitted Radiation (SUMER) instrument on board *SOHO* was presented by Judge et al. (2003). By comparing the measured intensities with synthetic data from simulations of acoustic waves, they conclude that even the lowest observed levels need to have a magnetic heating component in addition to heating by the dissipation of acoustic waves, thus questioning the common thought that the basal flux from stellar chromospheres is accounted for by non-magnetic heating.

With the advent of detailed, 3D radiation magnetohydrodynamic (RMHD) models spanning from the convection zone to the corona it has become possible to study the formation of spectral diagnostics in an inhomogeneous and dynamic setting. Such studies provide a more extensive understanding of how the atmospheric properties are encoded in the detailed line-profiles than the earlier studies based on 1D semi-empirical models. In the first papers in this series on the formation of *IRIS* diagnostics, we have employed this approach to study the Mg II h and k lines (Leenaarts et al. 2013a, 2013b; Pereira et al. 2013) and the Mg II triplet lines (Pereira et al. 2015). We will now present results for the C II lines. To make 3D non-LTE radiative transfer computationally feasible, it is crucial to have a model atom with as few levels as possible while retaining the main physical processes. In this first paper, we develop such a model atom and we study the general formation properties of the intensity profiles of the C II lines. In the next paper, we will present statistical correlations between the atmospheric parameters and observables. In the third paper on the C II lines, we will use *IRIS* observations to further test the diagnostic potential of the C II lines and use the comparison of observations with the synthetic observables to draw conclusions on what might be missing physical ingredients in the simulations.

The layout of this paper is as follows. In Section 2, we give details on how we solve the coupled equations of statistical equilibrium and radiative transfer. In Section 3, we describe the various model atmospheres we use. In Section 4, we describe the model atom, the atomic data and the procedure that ends up with a quintessential model atom. In Section 5, we present the general formation properties of the C II lines. In Section 6, we discuss the formation in a sunspot atmosphere and we end with conclusions and discussion in Section 7.

2. RADIATIVE TRANSFER

For the detailed analysis of the C II lines, we solve the statistical equilibrium equations in non-LTE using three codes. For the study of our atomic model, basic radiative transfer processes, and the simplifications of the model atom, we use the 1D code MULTI (Carlsson 1986). In order to study 3D effects, we use the full 3D radiative transfer code MULTI3D (Leenaarts & Carlsson 2009). To study the importance of partial redistribution (PRD) effects and effects of calculating background continua with several elements in non-LTE simultaneously, we use the code RH (Uitenbroek 2001). MULTI solves the non-LTE radiative transfer problem in semi-infinite, plane parallel 1D atmospheres with prescribed macroscopic velocity fields. Complete frequency redistribution (CRD) is assumed for all bound–bound transitions and the background scattering is considered to be coherent. Line transitions that overlap in frequency are not treated self consistently (which is of relevance here since one of the C II lines is a blend with two components). Version 2.3 of MULTI includes the local approximate operator of Olson et al. (1986), whereas Ng acceleration (Ng 1974), collisional-radiative switching (Hummer & Voels 1988), and the opacities are taken from the Uppsala Opacity Package (Gustafsson 1973). The background continuum opacity is normally calculated assuming LTE for the relevant atoms and ions, but it is possible to iteratively include non-LTE populations for the background opacity.

The full three-dimensional (3D) radiative transfer code MULTI3D is not only superior in that it treats the non-LTE problem in full 3D but the treatment of overlapping lines and continua is self-consistent and not based on iteration. However, the computations are naturally more computationally intensive in 3D, which is why we use the 1D version for experimentation with large model atoms. We also assume CRD for the computations with MULTI3D.

RH is another non-LTE code capable of treating PRD in the lines and calculating overlapping continua by solving for

several elements in non-LTE simultaneously. This code is therefore used for the tests of the significance of PRD and for the detailed continuum calculations.

3. MODEL ATMOSPHERES

We use a number of different model atmospheres in this work. We start by studying the atomic processes important for the lines we are interested in by using the often used semi-empirical VAL3C model atmosphere (Vernazza et al. 1981). Once we have arrived at a simplified atomic model that preserves the important characteristics of the more extended atomic model, we employ a 3D model atmosphere to test the simplified model atom over a wider parameter range and to see the sensitivity of the line formation to atmospheric properties. To study radiative transfer effects in 3D, we employ the full 3D solution. The 3D atmosphere is taken from a 3D simulation with the *Bifrost* code (Gudiksen et al. 2011). *Bifrost* solves the equations of RMHD on a staggered Cartesian grid. Detailed radiative transfer is included through the multi-group opacity approach (Nordlund 1982) modified to take into account scattering (Skartlien 2000). Radiative losses in the chromosphere are calculated in non-LTE using simplified recipes (Carlsson & Leenaarts 2012) that are based on detailed 1D full non-LTE radiative transfer simulations. Non-equilibrium ionization of hydrogen is included following the description of Leenaarts et al. (2007). The simulation we use encompasses $24 \times 24 \times 16.8$ Mm on the Sun discretized onto a $504 \times 504 \times 496$ grid. Vertically, the computational volume extends from 2.4 Mm below to 14.4 Mm above average optical depth unity at 500 nm (which is the zero-point of our height-scale), and thus covers the solar atmosphere from the upper convection zone, photosphere, chromosphere to the lower corona. Horizontally, the grid is equidistant with a spacing of 48 km. The z axis is not equidistant. It has grid spacing of 19 km between $z = -1$ and $z = 5$ Mm, whereas the spacing increases toward the lower and upper boundaries to a maximum of 98 km at the coronal boundary. Magnetic fields are introduced into a relaxed hydrodynamic simulation by specifying the vertical magnetic field at the bottom boundary with a potential field extrapolation producing the magnetic field throughout the 3D box. In our particular simulation, we specify two concentrations of opposite polarities separated by 8 Mm. The potential field is quickly swept to the intergranular lanes and slowly builds up a set of loops between the opposite polarities. We have chosen a snapshot at a time of 3850 s after the magnetic field was introduced, well after initial transients have passed through the box and the heating of the atmosphere through the work of the convection on the magnetic field has come to a quasi-steady state. This simulation is described in detail in Carlsson et al. (2015) and is the same as those used in Leenaarts et al. (2012), Štěpán et al. (2012), de la Cruz Rodríguez et al. (2013), and for the first papers in this series on the formation of IRIS diagnostics (Leenaarts et al. 2013a, 2013b; Pereira et al. 2013, 2015).

The vertical magnetic field strength in the photosphere is shown in Figure 1. The two opposite magnetic field polarity patches are clearly seen. We will illustrate formation properties along a slice through the model at $x = 12$ Mm, marked with a vertical line, and at four different positions, marked with letters A–D in Figure 1.

To study the formation of the C II lines also in a more active atmosphere, we employ a semi-empirical atmosphere of a sunspot umbra. The standard model SPOTM of Maltby et al. (1986) emphasizes the temperature structure of the photosphere up to the temperature minimum region and does not extend high enough to cover the formation region of the C II lines. We therefore use the semi-empirical model of Lites & Skumanich (1982) that is based on *OSO*-8 observations of the chromospheric lines of hydrogen (Lyα, Lyβ), Mg II (k, h), Ca II (K, H), and the transition region C IV 1548 nm resonance line.

The temperature structures of the two semi-empirical models and the four columns in the *Bifrost* snapshot are shown in Figure 2. Both the semi-empirical models have artificial temperature plateaus at 24 kK in order to get enough flux in the hydrogen Lyα line. The umbral model has this plateau and the transition region at a slightly smaller column mass than the quiet-Sun model VAL3C. The transition region in the *Bifrost* model is typically at an even smaller column mass.

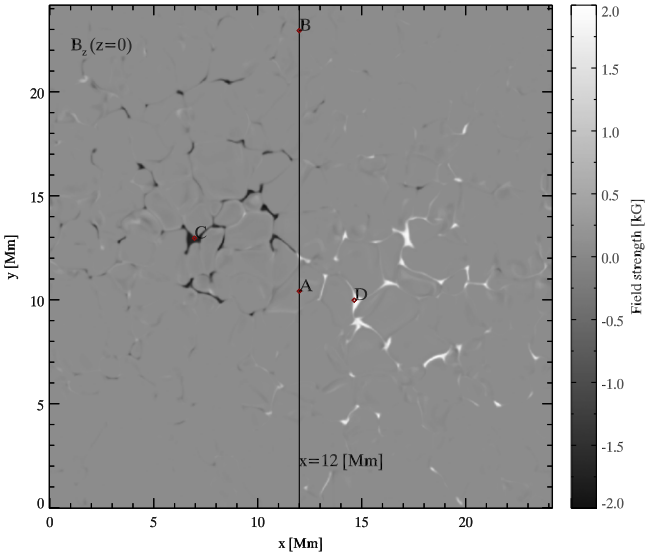

Figure 1. Vertical magnetic field of the *Bifrost* atmosphere at $z = 0$ height. The vertical line shows the position of the 2D cut used and the letters A–D mark columns chosen for detailed study in Section 5.1.

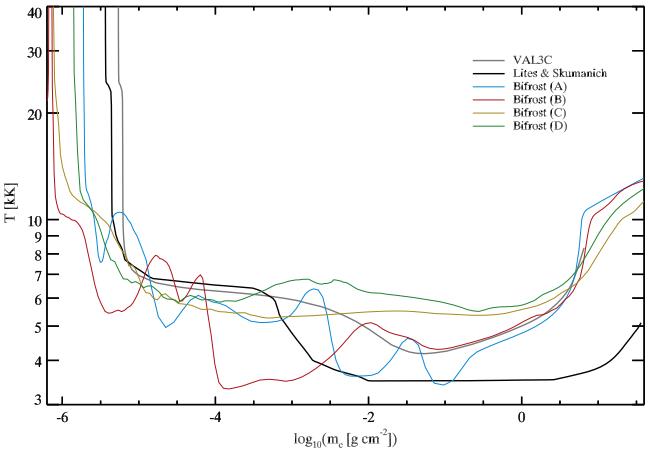

Figure 2. Temperature as a function of logarithmic column mass for atmospheric models in this paper. The quiet-Sun model VAL3C (thick gray), the umbral model of Lites & Skumanich (1982; thick black), and four columns from the *Bifrost* snapshot as marked in Figure 1: A (blue), B (red), C (brown), and D (green).

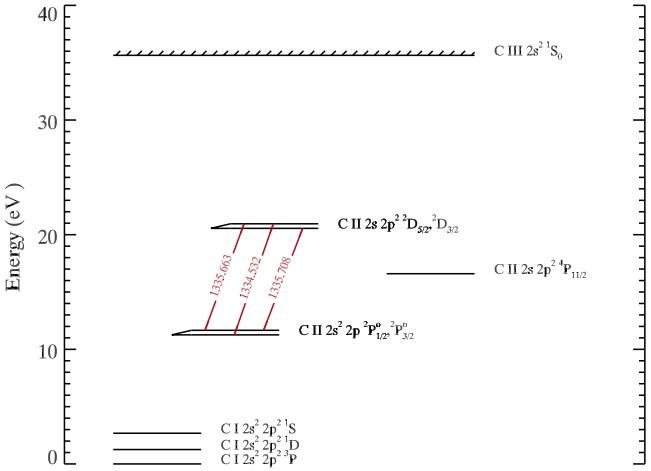

Figure 3. C II atomic model with nine levels. The C II multiplet of special interest here consists of the three allowed transitions between the $2s\ 2p^2\ ^2D$ and the $2s^2\ 2p\ ^2P^o$ terms.

4. QUINTESSENTIAL MODEL ATOM

One of the objectives of the current work is to arrive at a simplified model atom that includes the non-LTE processes important for the formation of the intensity profiles of the C II 133.5 nm lines but is small enough to enable large-scale 3D non-LTE simulations. To that end, we start with a more complex model atom: the one used by Judge et al. (2003). This atomic model contains a total of 22 levels: 8 levels of C I, 6 levels of C II, 4 levels of C III, 3 levels of C IV, and the ground state of C V. We simplify this model by removing and merging levels following the procedure described in Bard & Carlsson (2008). At each step, we solve the non-LTE problem and compare the intensities in the C II 133.5 nm lines and the ionization fraction as a function of depth with that of the full model atom. As a first step, we remove all levels above the ground state of C III. This results in a model atom of 15 levels. In the next step, we remove levels not important for the ionization balance and the levels not directly coupled to the lower and upper levels of the C II 133.5 nm lines. The quintessential model atom we arrive at has a total of nine levels, see Figure 3. The lines we are interested in are the unblended component at 133.4532 nm (hereafter called the 133.4 nm line) and the stronger 133.5708 nm line that has a weaker blend at 133.5663 nm, hereafter collectively referred to as the 133.5 nm line. A comparison between the results for the VAL3C atmosphere based on the 22-level model atom and the 15 and nine-level atoms is given in Figure 4. Both the intensities and ionization structure are almost identical, calculated from the quintessential nine-level model atom as from the full 22-level atom. This is also true for the full *Bifrost* atmosphere—on average, the quintessential nine-level model has 5% larger peak intensity in the C II lines but less than 5% of the columns show a difference of more than 15% and the largest difference is 27% compared with the full 22-level atom.

We have also made experiments with a more complete C I model atom including highly excited levels to get recombination channels right and including the photoionizing radiation from the hydrogen Lyα line. This influences the C I/C II balance at the low temperature end, but has negligible influence on the C II 133.5 nm lines, see Section 4.3.

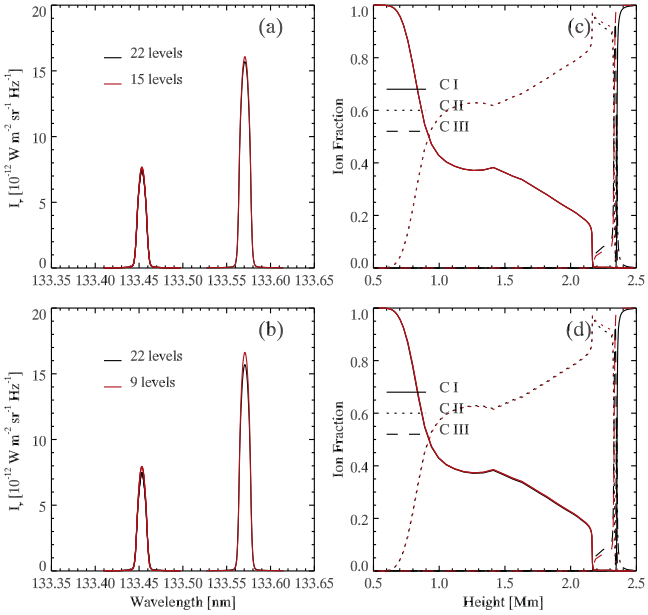

Figure 4. Intensities and ionization fractions resulting from the original 22-level atom and the simplified 15-level atom (panels (a) and (c)) and the quintessential nine-level atom (panels (b) and (d)). Results for the reference model are shown in black and for the 15/9-level models in red. The VAL3C model atmosphere was used and the weak blend at 133.566 nm was neglected.

We stress that our model atom has been constructed for the specific purpose of modeling the intensity of the C II 133.5 nm lines. If other lines are of interest or if polarization is to be calculated, this model atom might need to be extended to include additional levels.

4.1. Atomic Data

In the nine-level atomic model, level energies for C I are from the NIST[1] online database, the C II level is from Moore et al. (1993) and the C III level is from Martin et al. (1978). The transition probabilities are from the NIST database. Detailed photoionization data (from C I to C II) are from the TOPBASE[2] database of the OPACITY project. The bound–bound collisional rates for C II are from Tayal (2008). The bound–bound collisional rates for neutral carbon are determined using the impact parameter method of Seaton (1962). As we will see later, the intensity ratio between the multiplet components depends on the relative population of the upper levels. As the energy difference between the levels of the $2p\ ^2D$ term is only 2.5 cm^{-1} (0.008 eV), collisions with neutral hydrogen may be important. For these collisions, we use data from Bahcall & Wolf (1968) with $P(i \rightarrow f) = 4/10$ (Barklem 2014, private communication).

In our simulations, the total recombination rates include the radiative rates, dielectronic recombination rates, and three body recombination rates. The radiative recombination rates are either calculated from the detailed photoionization cross-sections (recombination into C I) or as tabulated by Shull & van Steenberg (1982). The three body recombination rates are from Arnaud & Rothenflug (1985) and the dielectronic recombination rates are from Altun et al. (2004; C II → C I) and Colgan et al. (2003; C III → C II). We set the carbon

[1] http://physics.nist.gov/PhysRefData/ASD/html/vernist.shtml
[2] http://cdsarc.u-strasbg.fr

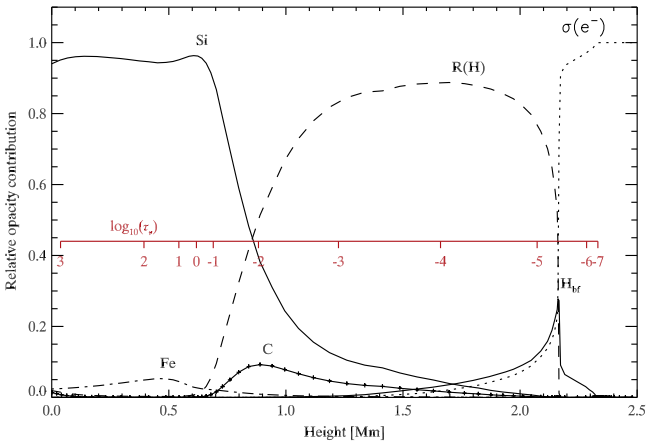

Figure 5. Relative contribution to the background opacity at 133.5 nm as a function of height in the VAL3C atmosphere. The source of the opacity is bound-free opacity from Si, C, Fe, and H and electron scattering ($\sigma(e^-)$) and Rayleigh scattering on neutral hydrogen (R(H)). The secondary height scale shown in red is the logarithm of the continuum optical depth at 133.5 nm. Hydrogen, carbon, and silicon have all been treated in non-LTE while iron was treated in LTE.

abundance to 8.43 (Asplund et al. 2009) on the usual logarithmic scale where the abundance of hydrogen is 12.

4.2. Continuum Intensity

In addition to the opacity from the multiplet lines we are interested in, we have a background opacity that varies slowly with wavelength. At 133.5 nm under solar chromospheric conditions, this background opacity is dominated by bound-free transitions in silicon, carbon, hydrogen, and iron with electron scattering taking over as the dominant background opacity source in the upper chromosphere and corona, see Figure 5. The carbon background opacity comes from bound-free transitions from the levels $2p^2\ ^1D$ and $2p^2\ ^1S$ while the ground term $2p^2\ ^3P$ has a bound-free edge at 110 nm and does not contribute. Note that the energy difference from the S I levels $3p^4\ ^1D$ and $3p^4\ ^1S$ and the ground state of S II places the bound-free edges longward of our carbon multiplet and these transitions would then contribute to the background opacity. However, these levels ionize to an excited state of S II placing the bound-free edges shortward of our multiplet and sulphur, therefore, does not contribute significantly to the background opacity. Hydrogen, carbon, and silicon are all out of LTE in the chromosphere, so a proper calculation of the continuum intensity needs to treat all three elements in non-LTE simultaneously. Our carbon model atom includes the singlet levels of C I so that contribution is in non-LTE automatically. Hydrogen non-LTE level populations are also provided in the atmospheric models used here so the only remaining problem is the silicon contribution. To include silicon in non-LTE simultaneously with carbon would be computationally costly. This is of course necessary if one is interested in getting the continuum intensity correct. However, in cases where the continuum intensity is very much lower than the carbon multiplet intensity, the correct treatment of the background continuum may be unimportant for getting the correct multiplet intensity. We tested this by comparing the full treatment with one where silicon is assumed to be in LTE for the calculation of the background opacity, see Figure 6. It is clear that the continuum intensity is severely overestimated when silicon is

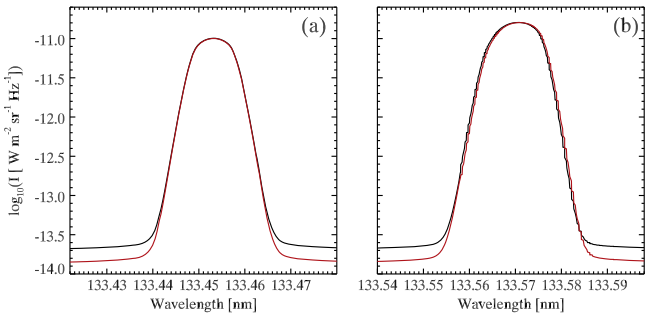

Figure 6. C II line intensity for the C II 133.4 nm (left) and C II 133.5 nm (right) lines, when assuming non-LTE Si background opacity (red) and LTE Si background opacity (black). The VAL3C atmosphere was used for the comparison. Note the logarithmic intensity scale.

treated in LTE, but that such a simplified treatment does not significantly affect the line intensity.

4.3. Ionization Balance

The formation of the C II-lines is to a large extent set by the ionization balance—where in the atmosphere is the C II ionization stage dominant? This in turn is set by the ionization and recombination rates between C II and C III and by the rates between C I and C II. The balance between C I and C II is dominated by photoionization and radiative recombination. To get this balance right, we must include the levels that dominate the photoionization (normally the ground levels and levels with low excitation) and highly excited levels that dominate in the recombination channels. The photoionization of C I is dominated by ionization from the $2p^2\ ^3P$ term with edges around 110 nm and from the $2p^2\ ^1D$ level with photoionization edges close to 123.9 nm. For the latter, photoionization from hydrogen Lyα radiation may play an important role. This complicates the computational task enormously since the proper solution involves a large number of C I energy levels and the simultaneous solution of the hydrogen non-LTE problem with the Lyα line treated in partial frequency redistribution. We have made test calculations with such a setup and find that by neglecting the photoionization from Lyα and all levels above the ground term and the two first excited levels of C I, the amount of C II at temperatures below 10 kK is indeed underestimated, but the effect on the C II lines is minimal (intensity changes by less than 5%).

In the classical coronal ionization equilibrium approximation, photoionization is neglected and the ionization rate is assumed to be dominated by collisional ionization. This leads to a severe underestimate of the amount of C II below a temperature of 20 kK under solar chromospheric conditions, as is clearly shown in Figure 7.

At the high temperature end, the ionization fraction of C II is determined by collisional ionization and dielectronic recombination. Part of the dielectronic recombination is to high energy levels and there may be collisional ionization taking place before the electron cascades down to lower energy levels through allowed radiative transitions. A correction in the dielectronic recombination rates is made following Summers (1972) as implemented by Judge (2007) by including a density dependent factor in the dielectronic recombination coefficient. This decreases the recombination rate and we get a smaller C II fraction at the high temperature range than if the dielectronic recombinations to high energy C II-levels are all assumed to end

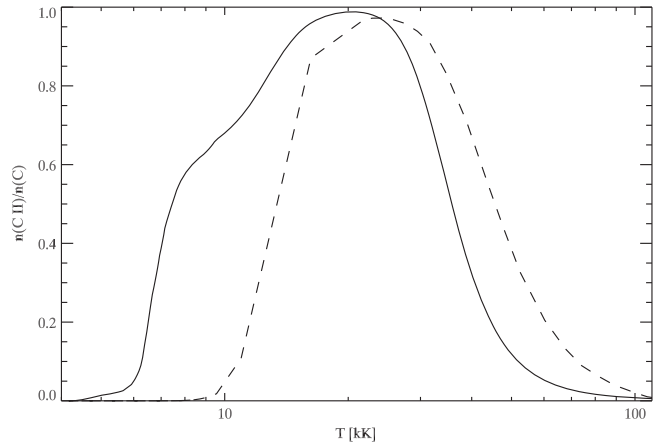

Figure 7. C II ionization fraction in the VAL3C model atmosphere using the adopted atomic parameters (solid), neglecting photoionization from C I to C II, and also neglecting density dependent dielectronic recombination (=default Chianti ionization balance; dashed). Note the logarithmic temperature scale.

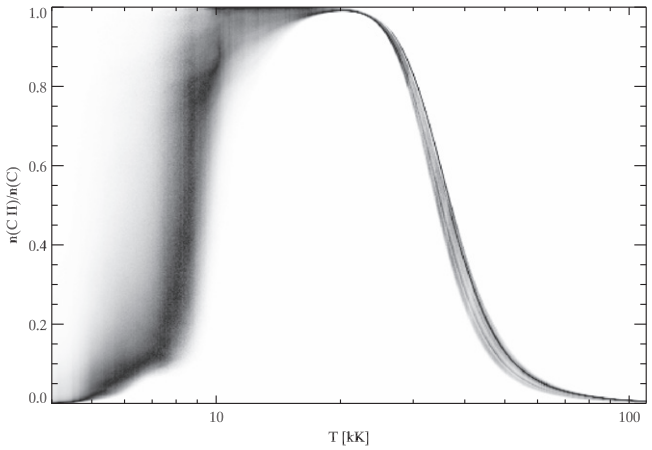

Figure 8. Probability density function of the C II ionization fraction as function of temperature in the *Bifrost* simulation. In each temperature bin, the PDF has been normalized to the largest value for increased visibility. Note the logarithmic temperature scale.

up with radiative cascades to the ground state, see Figure 7. Neglecting Summer's correction factor for dielectronic recombination, the C II ionization fraction does not fall below 10% until a temperature of 75 kK is reached. Including this factor, the fraction of C II drops rapidly at a temperature of 25 kK and we have an ionization fraction below 10% already at 50 kK.

The radiative and dielectronic recombination rates are a function of temperature and linearly dependent on electron density apart from the above mentioned density correction of the dielectronic recombination rate. Therefore, if the ionization is dominated by collisional ionization (also a function of temperature and linear in electron density) and three body recombination is negligible, the ionization balance is a function of temperature only. In Figure 8, we show the fraction of C II in the full *Bifrost* snapshot ($504 \times 504 \times 496$ grid points). It is clear that in the high temperature end we are close to having an ionization balance only dependent on temperature. The spread is caused by three-body recombination and the density dependent dielectric recombination. At the low temperature end, the ionization is dominated by photoionization and the ionization fraction is not a single valued function of temperature. There is also an extra spread caused by the 3D radiation field.

4.4. Effect of Partial Frequency Redistribution

The C II lines are resonance lines (lower levels of the ground term) and one might expect effects of partial frequency redistribution of photons (PRD) to be important. We tested this by solving the non-LTE problem for given atmospheres both including PRD effects and using the computationally advantageous approximation of complete redistribution (CRD). We did not find any significant differences, see Figure 9, and conclude that CRD can be used in the modeling of the C II 133.5 nm lines under solar conditions.

4.5. Importance of 3D Radiative Transfer

Figure 10 shows a comparison of the vertically emergent intensity in the core of the C II 133.4 nm line, solving each column in the 3D atmosphere independently as a 1D problem and solving the full 3D radiative transfer problem. It is clear that 3D scattering effects are important in the core of the line

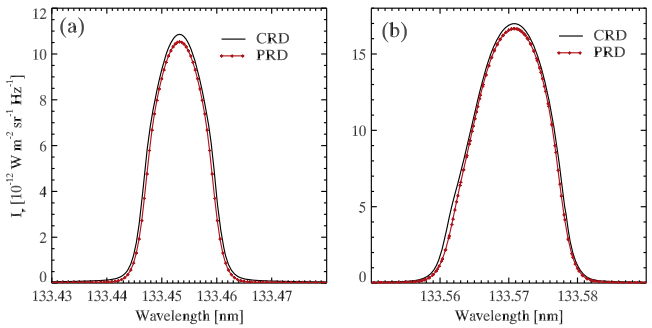

Figure 9. Comparison between partial redistribution (PRD, red) and complete redistribution (CRD, black) approximation for the C II lines in the VAL3C atmosphere for the C II 133.4 nm line (a) and C II 133.5 nm blend (b).

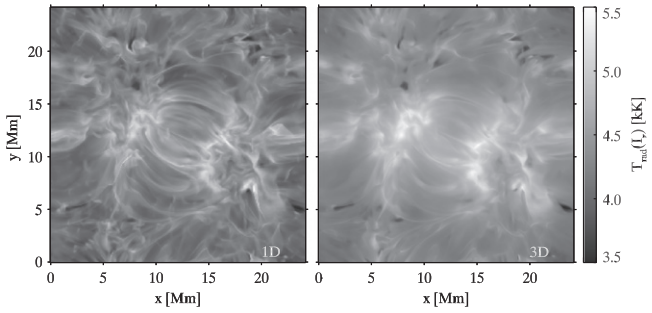

Figure 10. Comparison of the vertically emergent intensity in the core of the C II 133.4 nm line solving each column in the 3D atmosphere independently as a 1D problem (left) and solving the full 3D radiative transfer problem (right).

and a full 3D transfer solution should be employed. It also means that we should expect the intensity close to the core to be influenced by the surroundings and not provide a very accurate mapping of the conditions along the local column.

5. RESULTS

In this section, we will study in detail how the C II lines at 133.5 nm are formed. We use the quintessential nine-level model atom described above, assuming CRD but using the full 3D solution for the *Bifrost* atmosphere results.

5.1. Contribution Function to the Intensity

As a tool to find out which parts of the atmosphere contribute to the emergent intensity of the C II lines, we use the contribution function to intensity.

The emergent intensity in a 1D plane parallel semi-infinite atmosphere can be written as

$$I_{\nu,\mu} = \int_0^\infty \frac{1}{\mu} S_\nu(z) e^{-\tau_\nu(z)/\mu} \chi_\nu dz. \quad (1)$$

In this equation, $\mu = \cos\theta$, where θ is the angle between the line of sight to the observer and the local vertical. The source function (S_ν), opacity (χ_ν), and optical depth (τ_ν) are functions of frequency (ν) and geometrical height (z). At disk center ($\mu = 1$), the integrand in Equation (1) describes the local creation of photons ($S_\nu \chi_\nu dz$) and the fraction of those that escape ($e^{-\tau_\nu}$). It is thus natural to define the contribution function to intensity on a geometrical height scale as

$$C_{I_\nu}(z) = S_\nu e^{-\tau_\nu} \chi_\nu. \quad (2)$$

Following Carlsson & Stein (1997), we also rewrite the contribution function as

$$C_{I_\nu}(z) = S_\nu \tau_\nu e^{-\tau_\nu} \frac{\chi_\nu}{\tau_\nu}, \quad (3)$$

where the term $\tau_\nu e^{-\tau_\nu}$ having a maximum at $\tau_\nu = 1$ represents the Eddington–Barbier part of the contribution function, S_ν gives the source function contribution and the final term, $\frac{\chi_\nu}{\tau_\nu}$ picks out effects of velocity gradients in the atmosphere.

To illustrate the range of line formation scenarios, we have picked four different columns from the *Bifrost* atmosphere. These columns are marked in Figure 1.

Figures 11–14 show the total contribution function as functions of height and frequency across the C II 133.4 nm line (bottom right panels) as well as the three individual terms above in the same manner as in the four-panel diagrams in Carlsson & Stein (1997) for these four columns. To avoid the confusion from the blend we have chosen the 133.4 nm line to analyze the formation in detail but the same general characteristics are true for the stronger line as well, but with a formation a bit higher in the atmosphere.

Figure 11 shows a typical case of a double peaked profile (the intensity profile is shown in the bottom right panel). The velocity (turquoise almost vertical line in all panels) does not exhibit strong gradients, which is why the χ_ν/τ_ν term in the upper left panel does not exhibit strong variations with wavelength or height. The $\tau_\nu = 1$ (red dashed line in all panels) ranges from 0.8 Mm in the continuum to 2.1 Mm at line center. The source function (solid green line in the upper right panel) is equal to the Planck function (the dashed yellow line shows the radiation temperature of the Planck function and thus the temperature itself) from the photosphere up to a height of 0.7 Mm where it decouples. The strong peak in temperature at a height of 1.6 Mm causes a peak in the source function (not so pronounced in the radiation temperature representation shown with the green line, but quite evident in the linear representation shown in the image in the upper right panel). This peak in the source function is responsible for the two emission peaks in the intensity profile. Because of the lack of strong velocity gradients, the intensity profile is quite symmetric with almost equal intensity of the read and blue peaks. The line core is formed at the highest height of the optical depth unity curve at 2.1 Mm. The source function there is lower than at 1.6 Mm and we get a central reversal. At a height of 2.1 Mm, there is a downward velocity of 2 km s^{-1}, which causes a redshift of the line center with a similar amount.

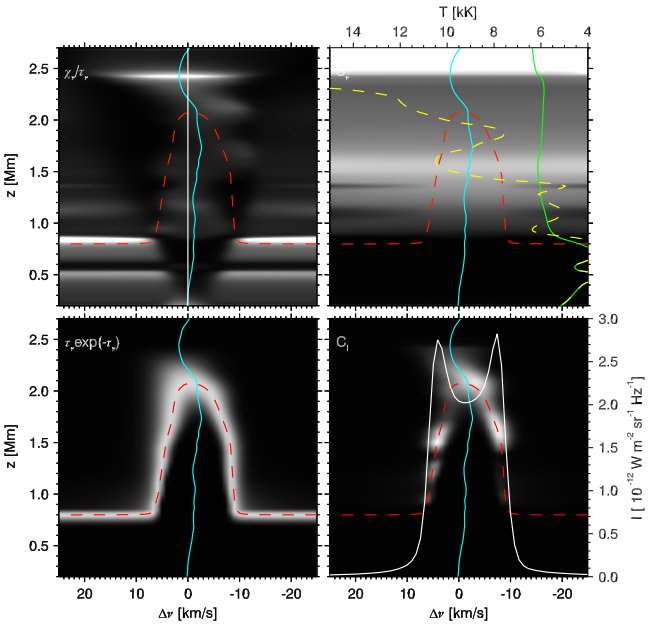

Figure 11. Contribution function to intensity of the C II 133.4 nm line. Each panel shows the quantity specified in the top-left corner as a grayscale image as functions of frequency from line center (in Doppler shift units) and atmospheric height z, see Equation (3). Multiplication of the first three produces the contribution function to intensity shown in the lower right panel. A $\tau_\nu = 1$ curve (red dashed) and the vertical velocity (turquoise solid, positive is upflow) are shown in each panel, with a $v_z = 0$ line in the upper left panel for reference. The upper right panel also contains the Planck function (yellow dashed) and the total source function (green solid) in radiation temperature units specified along the top. The lower right panel also contains the emergent intensity profile (white solid), with the scale along the right-hand side. The formation diagram is shown for column $(x, y) = (12, 10.3)$ Mm in the *Bifrost* atmosphere (column (A) in Figure 1).

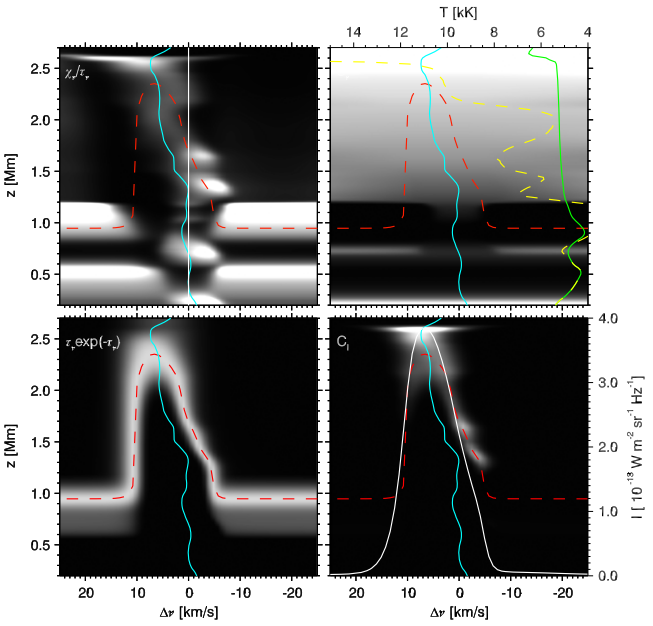

Figure 12. Same as Figure 11, but for column $(x, y) = (12, 22.8)$ Mm in the *Bifrost* atmosphere (column (B) in Figure 1).

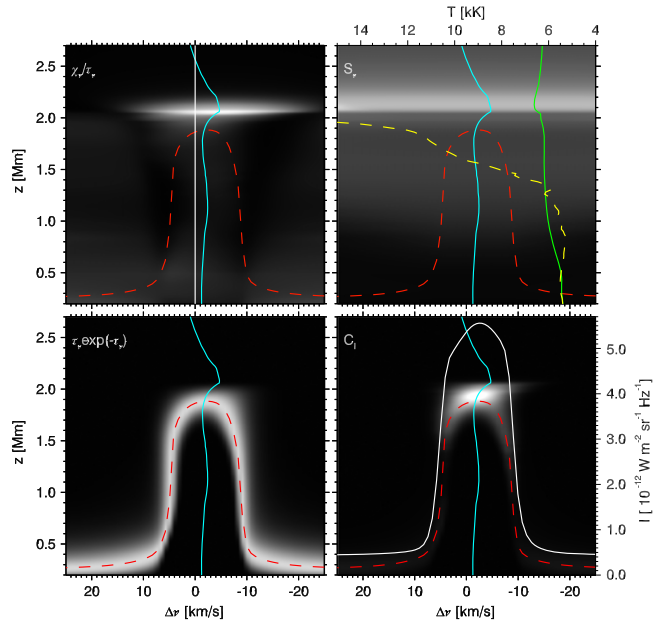

Figure 13. Same as Figure 11, but for column $(x, y) = (6.9, 12.9)$ Mm in the *Bifrost* atmosphere (column (C) in Figure 1).

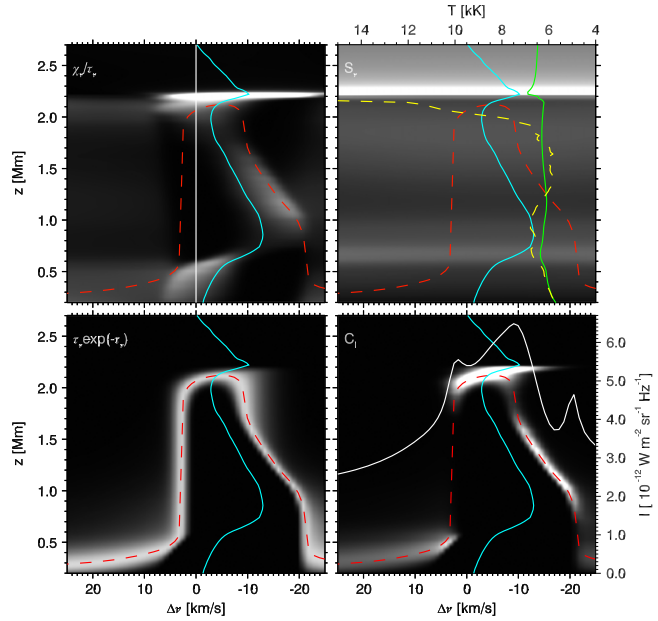

Figure 14. Same as Figure 11, but for column $(x, y) = (14.5, 9.9)$ Mm in the *Bifrost* atmosphere (column (D) in Figure 1).

Figure 12 shows a case of a single peaked profile where the formation is optically thin. It is clear from the total contribution function image (lower right panel) that the maximum of the contribution to intensity comes from a height of around 2.6 Mm, which is well above the maximum height of optical depth unity (2.3 Mm). The atmosphere is moving upward with 7 km s^{-1} where the intensity is formed and this gives a blueshift of the same amount. Note that the whole profile has a blueshift of 5–7 km s^{-1} even though the atmospheric velocity is almost zero below a height of 1.3 Mm. This is because most of the intensity profile is formed around a height of 2.6 Mm and not at the optical depth unity height. The asymmetry with a stronger red wing than blue wing comes from the velocity gradient giving a larger χ_ν/τ_ν term (upper left panel) on the red side. The FWHM of the intensity profile is 10.6 km s^{-1}, corresponding to the thermal broadening at 29 kK, which is consistent with the temperature in the lineforming region.

Figure 13 shows the formation of a single peaked profile in a flux concentration (column C in Figure 1 at $(x, y) = (6.9, 12.9)$ Mm). Because of the strong magnetic field (−1.6 kG in the photosphere), the density is lower than in the surroundings and a given optical depth occurs at a lower geometrical height. The continuum is therefore formed at 0.25 Mm compared with the average continuum formation height of 0.8 Mm. The core of the line is also formed slightly lower than in the surroundings, at 1.9 Mm height, but close to the height where the monochromatic optical depth is unity. The line thus shows an optically thick formation with the intensity being a map of the source function at optical depth unity. The source function is monotonically increasing with height up to where the core is formed, so there is no central depression. Also note the rather box-shaped profile—a consequence of a source function that increases more rapidly just above the continuum formation height than further up toward the core formation height.

Finally, Figure 14 shows the formation of the intensity in another flux concentration (column D in Figure 1 at $(x, y) = (14.5, 9.9)$ Mm). The continuum is formed low because of the strong magnetic field (1.7 kG in the photosphere). The continuum intensity is high because of the high temperature at optical depth unity in the continuum (see also Figure 2). Above the photosphere, we have strong velocity gradients that cause a broadened asymmetric profile. The source function is increasing up to a height of 0.6 Mm, is decreasing up to the height of optical depth unity at line center, and then shows a sharp increase. We therefore get a profile with three peaks with the outer ones formed at the wavelengths where optical depth unity is at 0.6 Mm. The FWHM of the intensity profile is 26.1 km s^{-1}, which is much larger than the thermal width in the line forming region. This is partly because of the large velocity gradients in the atmosphere at this column, but also because the profile calculated without velocity gradients in the atmosphere has a profile much broader than what would be expected from the thermal width. This is typical for a line that is formed in the optically thick regime. The line width depends strongly on how the source function varies with height in the atmosphere. We will return to this point in Section 5.2.

So far we have exemplified the formation of the C II 133.4 nm line through a detailed analysis of four different columns in the *Bifrost* atmosphere. We will now look at the formation of the intensity along the cut at $x = 12$ Mm (see Figure 1). We will investigate the contribution function to intensity at the line core, where, for each column in the simulation atmosphere, the line core is defined as the wavelength with maximum intensity (single peaked profiles) or minimum intensity in the central reversal (double peaked profiles). This contribution function is given in Equation (2). We are also interested in where the integrated intensity is coming from. We achieve this by defining the contribution function to total intensity as the integral over frequency of the contribution function to specific intensity:

$$C_{I_{\rm total}}(z) = \int C_{I_\nu}(z)\, d\nu. \quad (4)$$

Note that this definition only makes sense when the continuum intensity is much lower than the line intensity

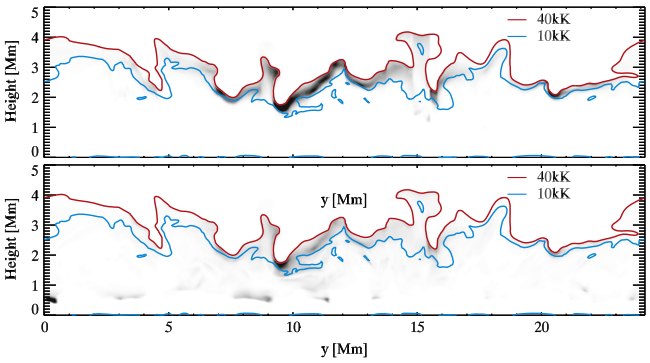

Figure 15. Contribution function to intensity at line core (top) and the contribution function to total intensity (bottom) on a height scale along the cut through the *Bifrost* atmosphere at $X = 12$ Mm shown as grayscale images. Temperature contours are given at 40 kK (red) and 10 kK (blue). The integration for the contribution function to total intensity was performed over ± 20 km s^{-1}.

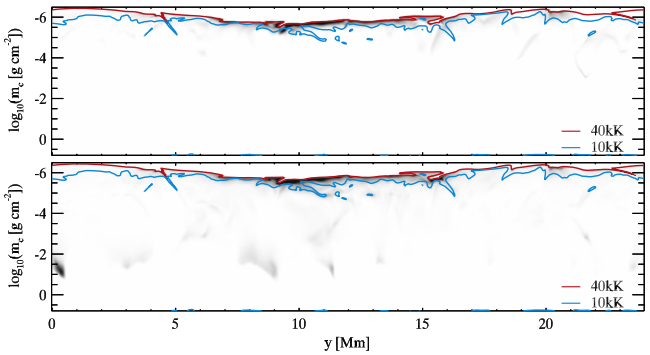

Figure 16. Same as Figure 15, but on a logarithmic column mass scale (see Equation (6)).

(which is the case here). We perform the integration over a wide enough frequency range to cover the width of the line but narrow enough not to be dominated by the continuum intensity contribution.

The top panel of Figure 15 shows the contribution function to the intensity at the line core along this cut. The line core is normally formed between 10 and 40 kK, but there are also regions where the line core contribution function reaches its maximum at lower temperatures (e.g., around $y = 17$–18 Mm). This happens when the transition region is at a low density. Optical depth unity is reached when we have high enough density. With a low density in the transition region, this happens deeper down where the temperature is lower. Because of the lower temperature, the line is also weaker (since the intensity is the integral of the contribution function, Figure 15 also gives an indication of the intensity). The formation layer of the line core is between 2 and 4 Mm in height and is as corrugated as the temperature structure.

The bottom panel of Figure 15 shows the contribution function to total intensity. The total intensity is mostly coming from the core formation region but there is also a broad tail of the contribution function going all the way down to the formation region of the continuum (which is, on average, around a height of 0.8 Mm). At $y = 0$–0.5 Mm the contribution function to total intensity is dominated by the continuum contribution. Here the continuum is enhanced because of a high temperature (up to 7 kK) around 0.8 Mm and the line is actually in absorption.

The height of unit optical depth (and therefore also the formation height) varies with the density stratification. Since the 133.5 nm lines are resonance lines, we expect the optical depth unity to be at a given column density of singly ionized carbon. The opacity at the line core depends on the broadening of the profile but is on the order of 10^6 cm^2 g^{-1} for the C II 133.4 nm line. We therefore expect optical depth unity to be at a column mass of about 10^{-6} g cm^{-2}. We can define a contribution function on a logarithmic column mass scale from

$$C_{I_\nu}\left(\log_{10} m_{\rm c}\right) d\left(\log_{10} m_{\rm c}\right) = C_{I_\nu}(z)\, dz \tag{5}$$

where $m_{\rm c}$ is the column mass, which leads to

$$C_{I_\nu}\left(\log_{10} m_{\rm c}\right) = \frac{m_{\rm c}}{\rho} \ln(10)\, C_{I_\nu}(z). \tag{6}$$

Figure 16 shows the contribution function to intensity at line core (top panel) as well as the contribution function to total intensity (bottom panel) on a logarithmic column mass scale. The range in logarithmic column mass has been chosen to correspond to the range in height for $y = 0$. This figure clearly illustrates that the corrugation of the transition region is much smaller on a column mass scale than on a height scale and that the contribution to intensity, both at line core and for the integrated total intensity, is concentrated to a small range in column mass. We can also see that indeed the contribution to intensity is around a column mass of 10^{-6} g cm^{-2}.

In sum, we expect line core diagnostics (especially the shift of the core) to give information from the region just below the transition region in the quiet-Sun. Diagnostics using the full line (like moments of the intensity) will be influenced by a much larger part of the chromosphere. We will return to the statistical correlation between various line shift diagnostics and the physical velocity in the simulation in Paper II (Rathore et al. 2015).

5.2. Line Width

For an optically thin line formed in the CRD regime, the width of the intensity profile is directly given by the width of the absorption/emission profile

$$\Phi_\nu = \frac{1}{\sqrt{\pi}\,\Delta\nu_D} e^{-\left(\frac{\Delta\nu}{\Delta\nu_D}\right)^2} \tag{7}$$

where $\Delta\nu$ is the difference in frequency from the line center frequency, ν_0, and

$$\Delta\nu_D = \frac{\nu_0}{c}\sqrt{\frac{2kT}{m} + \xi^2}, \tag{8}$$

where $\sqrt{2kT/m}$ gives the thermal Doppler broadening and ξ is a non-thermal velocity. Here k is the Boltzmann constant, m is the mass of the atom/ion, and we have assumed a Maxwellian velocity distribution at the temperature T. In an isothermal plasma and in the absence of a macroscopic velocity field, we get a symmetric Gaussian intensity profile with maximum intensity at ν_0 and a full-width of $2\Delta\nu_D$ at $1/e$ of the maximum intensity. Other popular measures of line width include the

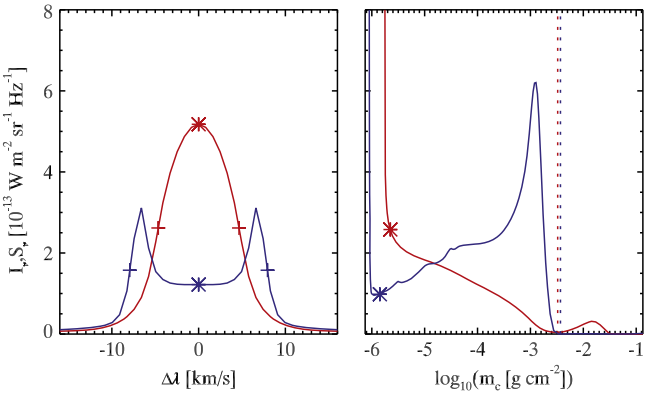

Figure 17. Intensity as a function of wavelength (given as equivalent velocity) at two columns in the *Bifrost* atmosphere with zero velocities (left) and corresponding source functions as a function of logarithmic column mass (right). The intensities at the line core are marked with asterisks in the left panel and the corresponding height for optical depth unity in the right panel. The heights for optical depth unity in the continuum are marked with vertical dotted lines. The points corresponding to the FWHM width are marked with plus-signs in the left panel with widths of 9.3 km s^{-1} (red) and 15.9 km s^{-1} (blue). The two positions are at $(x, y) = (12, 7.5)$ Mm (red) and $(x, y) = (12, 6.1)$ Mm (blue).

standard deviation, σ, of a Gaussian fit

$$I_\nu = \left(I_0 - I_c\right)e^{-\frac{\Delta\nu^2}{2\sigma^2}} + I_c, \tag{9}$$

the FWHM intensity ($W_{\rm FWHM}$), and the second moment of intensity

$$W_2 = \sqrt{\int (\nu - \nu_1)^2 \left(I_\nu - I_c\right) d\nu \Big/ I_{\rm tot}}\,, \tag{10}$$

where

$$I_{\rm tot} = \int \left(I_\nu - I_c\right) d\nu \tag{11}$$

is the zeroth moment and

$$\nu_1 = \int \Delta\nu \left(I_\nu - I_c\right) d\nu \Big/ I_{\rm tot} \tag{12}$$

is the first moment.

For a Gaussian intensity profile, we have the following relations between the four width measures:

$$\Delta\nu_D = \sqrt{2}\,\sigma \tag{13}$$

$$W_{\rm FWHM} = 2\sqrt{\ln 2}\,\Delta\nu_D \tag{14}$$

$$W_2 = \sigma. \tag{15}$$

For an optically thick line (as our C II lines) the situation is different. The width of the absorption profile still plays a role, but in addition the source function variation with depth is crucial. To illustrate this we have carried out a full 3D non-LTE calculation with the *Bifrost* atmosphere described earlier, but with all velocities set to zero. We thus have no effects from non-thermal velocities and the C II 133.4 nm intensity profile is symmetric. In Figure 17, we show the intensity profiles and corresponding source functions for two columns in this simulation. The red profile is illustrating a narrow, single-peaked profile where the source function increases almost linearly with decreasing logarithmic column mass from the point in the atmosphere where optical depth is unity in the continuum ($\log_{10} m_c = -2.5$) to optical depth unity in the core ($\log_{10} m_c = -5.6$). The temperature in the line-forming region is 11 kK, which gives a thermal broadening ($\sqrt{2kT/m}$) of 4 km s^{-1} and a thermal $W_{\rm FWHM} = 6.7$ km s^{-1}. For the red profile, we find $W_{\rm FWHM} = 9.3$ km s^{-1}, which is a factor 1.4 larger than the thermal width, even in this model where there are no non-thermal motions. This is sometimes called opacity broadening of an optically thick line. This broadening is dependent on the source function variation with depth. If the source function has a peak in the low atmosphere, just above the formation height of the continuum, we get steep emission flanks, a double peak intensity profile, and a larger width. The blue profile in Figure 17 is an example of such a scenario with $W_{\rm FWHM} = 15.9$ km s^{-1} with a temperature in the formation region of 9.6 kK.

We can get an estimate of the "opacity broadening" factor by using the Eddington–Barbier relation (that states that the emergent vertical intensity is equal to the source function at optical depth unity).

The optical depth is given by

$$d\tau_\nu = -\chi_\nu dz \tag{16}$$

where χ_ν is the opacity per volume. The column mass is given by

$$dm_c = -\rho dz \tag{17}$$

with ρ being the mass density. We thus have

$$d\tau_\nu = \frac{\chi_\nu}{\rho} dm_c \tag{18}$$

and we get the column mass where $\tau_\nu = 1$ at frequency $\Delta\nu$ from

$$1 = \int_0^{m_c(\Delta\nu)} \frac{\chi_\nu}{\rho} dm_c. \tag{19}$$

In an isothermal atmosphere with no non-thermal velocities, we have a constant atomic absorption profile and, for a resonance line of the dominant ionization stage, we get a constant line opacity per unit mass:

$$\frac{\chi_{l\nu}}{\rho} = \alpha_l e^{-\left(\frac{\Delta\nu}{\Delta\nu_D}\right)^2} \tag{20}$$

with α_l a constant. We assume the same to be true for the continuum opacity, χ_c (where $\chi_\nu = \chi_{l\nu} + \chi_c$). We then get

$$\frac{1}{m_c(\Delta\nu)} = \alpha_l e^{-\left(\frac{\Delta\nu}{\Delta\nu_D}\right)^2} + \frac{\chi_c}{\rho}. \tag{21}$$

Using the same equation for the continuum, $\Delta\nu \to \infty$, we can eliminate the χ_c/ρ term:

$$\frac{1}{m_c(\Delta\nu)} - \frac{1}{m_c(\infty)} = \alpha_l e^{-\left(\frac{\Delta\nu}{\Delta\nu_D}\right)^2}. \tag{22}$$

For the line center, $\Delta\nu = 0$, we get

$$\frac{1}{m_c(0)} - \frac{1}{m_c(\infty)} = \alpha_l. \tag{23}$$

This gives

$$\frac{\Delta\nu}{\Delta\nu_D} = \sqrt{\ln \frac{\frac{1}{m_c(0)} - \frac{1}{m_c(\infty)}}{\frac{1}{m_c(\Delta\nu)} - \frac{1}{m_c(\infty)}}}. \quad (24)$$

In the case of $m_c(\infty) \gg m_c(\Delta\nu)$, this reduces to

$$\frac{\Delta\nu}{\Delta\nu_D} = \sqrt{\ln \frac{m_c(\Delta\nu)}{m_c(0)}}. \quad (25)$$

For the blue profile in Figure 17, we have for the FWHM formation height $\log_{10}(m_c(\Delta\nu)) \approx -2.7$, $\log_{10}(m_c(0)) = -5.8$ and $\log_{10}(m_c(\infty)) = -2.4$. Using Equation (24), this gives an opacity broadening factor of 2.8, which is similar to the actual value of $15.9/6.1 = 2.6$. For the red profile, we get an opacity broadening factor of 1.9, which is larger than the actual value of 1.4. This is because the Eddington–Barbier relation underestimates the intensity peak when the source function is very steep and nonlinear in the line forming region and therefore overestimates the value of $m_c(\Delta\nu)$ that is necessary to reach optical depth unity. Equation (24) also gives the correct position of the emission peaks of the blue profile. We conclude that the width of the C II lines can be 1.4–3 times what is given by the width of the atomic absorption profile with larger values for double peaked profiles.

5.3. Intensity Ratio

The intensity ratio between the components in the multiplet gives an additional diagnostic value. Since the two levels within each term are very close in energy, collisions will be efficient in driving the population ratio toward the ratio of the degeneracies. The lower levels have a ratio of their degeneracies of two and our simulations confirm that the population densities have this ratio throughout the line forming regions. The opacity scales as $n_l f_{lu}$, where n_l is the population density of the lower level and f_{lu} is the absorption oscillator strength. The oscillator strengths of the two lines have a ratio of 0.9 such that the opacity in the 133.5708 nm line is a factor of 1.8 times that of the C II 133.4 nm line. In the optically thin limit, we have

$$I_\nu \simeq \int (\chi_{l\nu} + \chi_c) S_\nu ds. \quad (26)$$

In the coronal approximation (collisional excitation, radiative deexcitation), the source functions of the two lines are the same and the line opacity, $\chi_{l\nu}$, has the above ratio of 1.8 because the atomic absorption profiles are also identical. The intensity ratio is thus 1.8 at all frequencies across the line profiles where the line opacity dominates over the continuum opacity.

For an optically thick line, this is no longer true. We start by discussing the case of double peaked profiles and equal source functions. The two emission peaks of each line are formed at the local source function maximum and we therefore get equal peak intensities (but with a larger separation for the stronger C II 133.5 nm line). The self reversal is formed higher up where the source function is decreasing with height and the stronger line has its core formed higher and therefore has a lower core intensity. Single peak profiles mean that the source function is increasing with height and the C II 133.5 nm line will therefore have higher peak intensity than the C II 133.4 nm line. In general, the two source functions are *not* equal and we can, in principle, get any intensity ratio. The weakest blend shares an upper level with the C II 133.4 nm line, and since it becomes optically thin at a deeper level than the other lines, it tends to depopulate the upper level, decreasing the source function also of the C II 133.4 nm line. This source function difference tends to increase the intensity ratio between the lines.

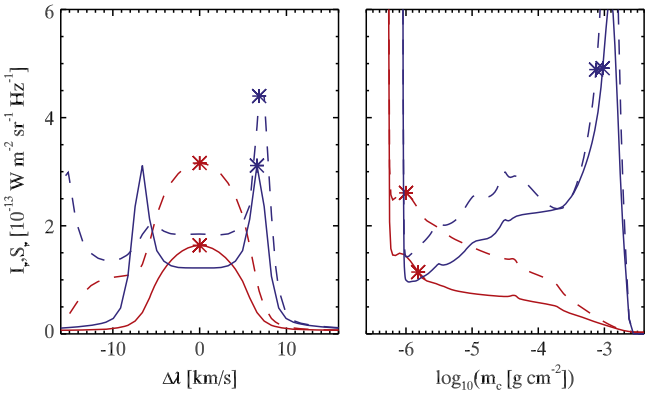

Figure 18. Intensity as a function of wavelength (given as equivalent velocity) at two columns in the *Bifrost* atmosphere with zero velocities (left) for the C II 133.4 nm line (solid) and the C II 133.5 nm line (dashed) and corresponding source functions as function of logarithmic column mass (right). Maximum intensities are marked with asterisks in the left panel and the corresponding height for optical depth unity in the right panel. The two *Bifrost* columns are at $(x, y) = (12, 21)$ Mm (red) and $(x, y) = (12, 6.1)$ Mm (blue).

We illustrate the dependency of the ratio on the source function behavior in Figure 18 where we show intensity profiles and source functions for the two lines at two locations in the *Bifrost* simulation. The velocities were set to zero before the Multi3D calculation of intensities. We thus get symmetric intensity profiles for the C II 133.4 nm line but asymmetric profiles for the C II 133.5 nm line because of the blend in the blue wing. The profiles in red were taken from the column at $(x, y) = (12, 21)$ Mm, where we have single peak intensity profiles (left panel). The locations of line core optical depth unity are marked on the source functions displayed in the right panel. The C II 133.5 nm line core (dashed line) is formed higher than the C II 133.4 nm line (lower column mass) and that would by itself give a higher core intensity since the source function is increasing with decreasing column mass. The main reason for the high intensity ratio of 1.9 is the large difference in the source functions. The profiles in blue were taken from the column at $(x, y) = (12, 6.1)$ Mm (same as the blue profile in Figure 17) where the intensity profile has two peaks. For the stronger C II 133.5 nm line, we do not reach low enough opacity on the blue (short wavelength) side of the stronger component to reach optical depth unity at the source function maximum depth and we need to go all the way to the blue side of the blend to get the corresponding intensity peak. This explains the rather weird profile (dashed blue line in the left panel). The red (long wavelength) peaks have an intensity ratio of 1.4, again mainly caused by differences in the source functions.

The source function differences are driven by radiative rates, both losses in the weakest line decreasing the source function of the C II 133.4 nm line that shares the upper level with the weak blend and absorptions of these photons in the C II 133.5 nm line (which lead to an increase of the C II 133.5 nm source function). Collisions between the upper $2p\ ^2D$ levels are not efficient enough to drive the source functions to equality.

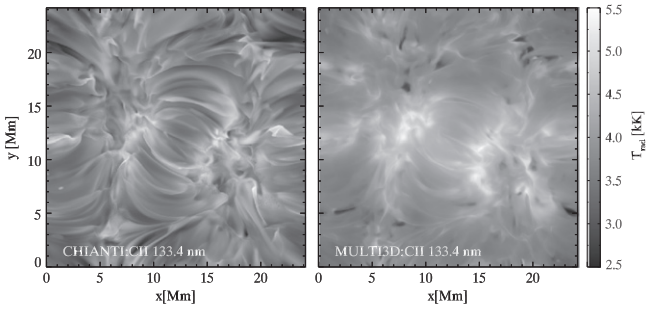

Figure 19. Emergent intensity at 133.4663 nm from the coronal approximation (left panel) and from the full 3D non-LTE calculation (right panel).

We have also included collisions with neutral hydrogen between these levels but a factor of 10 higher total collisional rates would be needed to significantly affect the source function ratios.

We conclude that the intensity ratio of the C II 133.5 nm and C II 133.4 nm lines is primarily indicating the ratio of the source functions of the lines. This ratio is normally larger than one but can have any value, including the optically thin value of 1.8. We expect a lower ratio when densities are high in the line forming region, as is the case for the intensity peaks of double peak profiles.

5.4. Comparison with Optically Thin Modeling

We have found that the C II lines are mostly formed in the optically thick regime. If we instead assume optically thin formation with the ionization equilibrium set by collisional ionization and dielectric recombination without density dependent effects (standard coronal approximation), we severely underestimate the amount of C II in the upper chromosphere and overestimate the amount in the higher temperature region (see Figure 7). In the optically thin regime, the intensity is set by the source function multiplied by the optical thickness of C II in the region. With the low densities where C II exists in the coronal approximation, this gives an optical thickness of less than 0.1. The source function then needs to be more than 10 times higher than what it is in our model at optical depth unity to give a similar intensity. This is normally not the case and we thus get a weaker line from the coronal approximation than in our non-LTE modeling. This is shown in Figure 19 where we compare the emergent intensity from assuming the coronal approximation (left panel) with our simulation employing the full 3D non-LTE modeling (right panel).

6. SUNSPOT MODEL

In addition to the quiet-Sun case, we have also studied the behavior of the lines in the sunspot model atmosphere of Lites & Skumanich (1982). The temperature structure of this model is shown in Figure 2. The photospheric temperature is naturally lower than in the quiet-Sun model VAL3C and a low temperature of 3.5 kK continues up to $\log_{10} m_c = -2$ where there is a rapid temperature increase to a chromospheric plateau of 6.5 kK, slightly above the VAL3C temperatures at corresponding column masses. There is a rapid temperature increase in the transition region at $\log_{10} m_c = -5.44$. A temperature plateau has been introduced at a temperature of 24 kK in order to get a Lyα flux similar to the observed flux.

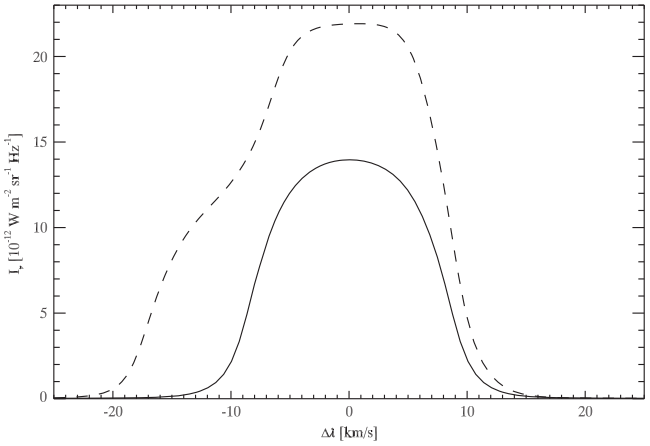

Figure 20. Intensity as a function of wavelength (in equivalent velocity units) for the C II 133.4 nm line (solid) and the C II 133.5 nm line (dashed) in the sunspot umbral model of Lites & Skumanich (1982).

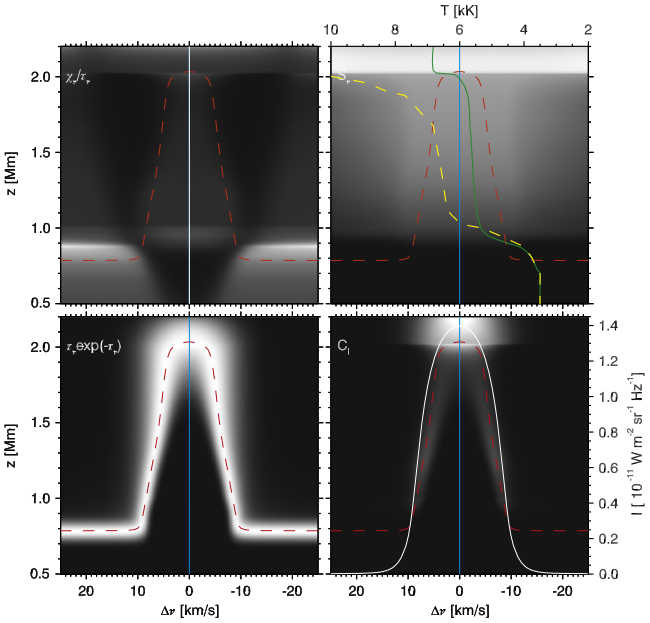

Figure 21. Same as Figure 11, but for the sunspot model atmosphere of Lites & Skumanich (1982).

The emergent intensity for the C II 133.5 nm lines is shown in Figure 20. The ratio of the maximum intensities of the two lines is 1.6. The line profiles deviate from a Gaussian shape in that the core part is flatter (especially for the stronger C II 133.5 nm line) and the flanks are steeper than the best-fit Gaussian. The FWHM of the intensity profile of the unblended C II 133.4 nm line is 16.4 km s^{-1}. The temperature at the formation height is 24 kK and the microturbulence in the sunspot model is 2.6 km s^{-1}. In an optically thin formation, the thermal width and the microturbulence would combine to give an FWHM of 10.5 km s^{-1}. We thus have an opacity broadening factor of 1.6.

The intensity formation of the C II 133.4 nm line in this atmosphere is shown in Figure 21. The velocities for this atmosphere are set to zero. The $\tau_\nu = 1$ height (red dashed line in all panels) ranges from 0.8 Mm in the continuum to 2.0 Mm at the line center. The source function (solid green line in the upper right panel) is equal to the Planck function (the yellow dashed line in the upper right panel) from the photosphere up to

0.9 Mm height where it decouples. The source function continuously increases with the increase in temperature and becomes maximum in the transition region. The monotonically increasing source function leads to a single peak emission line (the white curve in the lower right panel). The contribution function to intensity (image in the lower right panel) is concentrated around 2.1 Mm height around optical depth unity, which is also the lower part of the plateau at 24 kK in the model. Much of the line intensity is thus formed at the temperature plateau, which accounts for the rather flat line core. This is even more pronounced for the stronger C II 133.5 nm line where a significant fraction of the line core is formed at the temperature plateau where the source function is rather constant (upper left panel).

7. DISCUSSION AND CONCLUSIONS

The ionization balance and intensity profiles of the C II lines at 133.4–133.6 nm can be modeled with a nine-level model atom assuming complete frequency redistribution (CRD). The ionization balance C I/C II is dominated by photoionization and radiative recombination. The balance C II/C III is dominated by collisional ionization and dielectronic recombination. In the VAL3C atmosphere, carbon is more than 50% in the form of C II in the temperature range 5.6–35 kK, where especially the low temperature end is atmosphere dependent since it is set by photoionization, which is a non-local process. Horizontal scattering is important for the line core intensity, which necessitates 3D non-LTE modeling and makes line core diagnostics influenced by non-local conditions.

The line core is formed at temperatures 6–25 kK at a column mass close to 10^{-6} g cm^{-2}. The continuum formation is at 300–800 km and is dominated by background opacity from neutral silicon. This background opacity needs to be treated in non-LTE in order to get the continuum intensity right, but assuming LTE only affects the continuum intensity and not the line core intensity. The lower continuum formation height is for kilo-Gauss flux concentrations in the photosphere.

The atomic absorption profile width is set by thermal and non-thermal broadening. The emergent intensity profile is broader than the atomic absorption profile because of the optical thick formation. This excess "opacity broadening" is a factor of 1.2–4. The smaller opacity broadening happens for single peak intensity profiles that originate from a source function with a steep increase into the transition region and with a low chromospheric temperature. The larger opacity broadening is for double peak intensity profiles with central reversals that result from a source function with a local maximum in the lower chromosphere because of a steep temperature rise there.

The intensity ratio between the C II 133.5 nm and the C II 133.4 nm lines is lower than the optically thin value of 1.8 in the VAL3C model, the umbral model as well as for most columns in the *Bifrost* snapshot. The optically thick formation can give any ratio, depending on the ratio of the source functions of the two lines. The ratio is lower for double peak profiles where the intensity peaks are formed in the lower chromosphere than for single peak profiles formed in the transition region.

The C II lines are formed in the optically thick regime and erroneously assuming an optically thin formation using the coronal approximation (neglecting photoionization) leads to too high formation temperatures and too low intensities.

In the next paper in this series, we will discuss statistical correlations between atmospheric parameters and observables and explore the diagnostic potential of the C II lines.

The research leading to these results has received funding from the European Research Council under the European Union's Seventh Framework Programme (FP7/2007-2013)/ERC grant agreement No. 291058. This research was supported by the Research Council of Norway through the grant "Solar Atmospheric Modelling" and through grants of computing time from the Programme for Supercomputing. Bart De Pontieu and Jorrit Leenaarts are thanked for valuable comments on the manuscript.

REFERENCES

Altun, Z., Yumak, A., Badnell, N. R., Colgan, J., & Pindzola, M. S. 2004, A&A, 420, 775
Arnaud, M., & Rothenflug, R. 1985, A&AS, 60, 425
Asplund, M., Grevesse, N., Sauval, A. J., & Scott, P. 2009, ARA&A, 47, 481
Avrett, E., Landi, E., & McKillop, S. 2013, ApJ, 779, 155
Avrett, E. H., & Loeser, R. 2008, ApJS, 175, 229
Bahcall, J. N., & Wolf, R. A. 1968, ApJ, 152, 701
Bard, S., & Carlsson, M. 2008, ApJ, 682, 1376
Brown, A., & Carpenter, K. G. 1984, ApJL, 287, L43
Carlsson, M. 1986, Uppsala Astronomical Observatory Reports, A Computer Program for Solving Multi-level Non-LTE Radiative Transfer Problems in Moving or Static Atmospheres (Uppsala: Uppsala Astronomical Obs.), 33
Carlsson, M., & Leenaarts, J. 2012, A&A, 539, A39
Carlsson, M., & Stein, R. F. 1997, ApJ, 481, 500
Chipman, E. 1971, Harvard Univ., PhD thesis (Smithsonian Ap. Obs., Special Report No.338)
Colgan, J., Pindzola, M. S., Whiteford, A. D., & Badnell, N. R. 2003, A&A, 412, 597
Curdt, W., Brekke, P., Feldman, U., et al. 2001, A&A, 375, 591
de la Cruz Rodríguez, J., De Pontieu, B., Carlsson, M., & Rouppe van der Voort, L. H. M. 2013, ApJL, 764, L11
De Pontieu, B., Title, A. M., Lemen, J. R., et al. 2014, SoPh, 289, 2733
Detwiler, C. R., Garrett, D. L., Purcell, J. P., & Tousey, R. 1961, AnG, 17, 263
Gudiksen, B. V., Carlsson, M., Hansteen, V. H., et al. 2011, A&A, 531, A154
Gustafsson, B. 1973, Annaler, A Fortran Program for Calculating "Continuous" Absorption Coefficients of Stellar Atmospheres (Uppsala: Uppsala Astronomical Obs.), 5, 6
Hummer, D. G., & Voels, S. A. 1988, A&A, 192, 279
Judge, P. 2007, The HAO Spectral Diagnostic Package for Emitted Radiation (HAOS-DIPER) Reference Guide (Version 1.0), Tech. Rep. NCAR/TN-473+STR, the University Corporation for Atmospheric Research (UCAR)
Judge, P. G., Carlsson, M., & Stein, R. F. 2003, ApJ, 597, 1158
Leenaarts, J., & Carlsson, M. 2009, in ASP Conf. Ser. 415, The Second Hinode Science Meeting: Beyond Discovery-Toward Understanding, ed. B. Lites et al. (San Francisco, CA: ASP), 87
Leenaarts, J., Carlsson, M., Hansteen, V., & Rutten, R. J. 2007, A&A, 473, 625
Leenaarts, J., Carlsson, M., & Rouppe van der Voort, L. 2012, ApJ, 749, 136
Leenaarts, J., Pereira, T. M. D., Carlsson, M., Uitenbroek, H., & De Pontieu, B. 2013a, ApJ, 772, 89
Leenaarts, J., Pereira, T. M. D., Carlsson, M., Uitenbroek, H., & De Pontieu, B. 2013b, ApJ, 772, 90
Lites, B. W., Shine, R. A., & Chipman, E. G. 1978, ApJ, 222, 333
Lites, B. W., & Skumanich, A. 1982, ApJS, 49, 293
Maltby, P., Avrett, E. H., Carlsson, M., et al. 1986, ApJ, 306, 284
Martin, W. C., Zalubas, R., & Hagan, L. 1978, Atomic Energy Levels—The Rare-Earth Elements, (ESO)
Moore, C. E. 1993, in CRC Series in Evaluated Data in Atomic Physics, ed. J. W. Gallagher (Boca Raton, FL: CRC Press)
Ng, K.-C. 1974, JChPh, 61, 2680
Nordlund, A. 1982, A&A, 107, 1
Olson, G. L., Auer, L. H., & Buchler, J. R. 1986, JQSRT, 35, 431
Pereira, T. M. D., Carlsson, M., De Pontieu, B., & Hansteen, V. 2015, arXiv:1504.01733
Pereira, T. M. D., Leenaarts, J., De Pontieu, B., Carlsson, M., & Uitenbroek, H. 2013, ApJ, 778, 143
Pottasch, S. R. 1964, SSRv, 3, 816
Rathore, B., Carlsson, M., Leenaarts, J., & De Pontieu, B. 2015, ApJ, 811, 81

Schrijver, C. J. 1995, A&ARv, 6, 181
Seaton, M. J. 1962, PPS, 79, 1105
Shull, J. M., & van Steenberg, M. 1982, ApJS, 48, 95
Skartlien, R. 2000, ApJ, 536, 465
Štěpán, J., Trujillo Bueno, J., Carlsson, M., & Leenaarts, J. 2012, ApJL, 758, L43
Summers, H. P. 1972, MNRAS, 158, 255
Tayal, S. S. 2008, A&A, 486, 629
Uitenbroek, H. 2001, ApJ, 557, 389
Vernazza, J. E., Avrett, E. H., & Loeser, R. 1973, ApJ, 184, 605
Vernazza, J. E., Avrett, E. H., & Loeser, R. 1981, ApJS, 45, 635
Withbroe, G. L., & Noyes, R. W. 1977, ARA&A, 15, 363